Chinese Chemical Letters 35 (2024) 110031

Contents lists available at ScienceDirect

Chinese Chemical Letters

journal homepage: www.elsevier.com/locate/cclet

Coordination-based synthesis of Fe single-atom anchored nitrogen-doped carbon nanofibrous membrane for CO_2 electroreduction with nearly 100% CO selectivity

Xiujuan Wang[a,1], Yijie Wang[a,1], Luyun Cui[a], Wenqiang Gao[a], Xiao Li[a], Hong Liu[a,b,*], Weijia Zhou[a,*], Jingang Wang[a,*]

[a] Institute for Advanced Interdisciplinary Research (iAIR), University of Jinan, Ji'nan 250022, China
[b] State Key Laboratory of Crystal Materials, Shandong University, Ji'nan 250100, China

ARTICLE INFO

Article history:
Received 21 March 2024
Revised 16 May 2024
Accepted 19 May 2024
Available online 20 May 2024

Keywords:
CO_2 reduction reaction
Single atom
Electrospinning
Coordination structure
Carbon monoxide

ABSTRACT

Carbon-based materials with single-atom (SA) transition metals coordinated with nitrogen (M-N_x) have attracted extensive attention due to their superior electrochemical CO_2 reduction reaction (CO_2RR) performance. However, the uncontrolled recombination of metal atoms during the typical high-temperature synthesis process in M-N_x causes deterioration of CO_2RR activity. Herein, by using electrospinning, we propose a novel strategy for constructing a highly active and selective SA Fe-modified N-doped porous carbon fiber membrane catalyst (Fe-N-CF). This carbon membrane has an interconnected three-dimensional structure and a hierarchical porous structure, which can not only confine Fe to be single atom as active centers, but also provide a diffusion channel for CO_2 molecules. Relying on its special structure and stable mechanical properties, Fe-N-CF is directly used for CO_2RR, which presents an excellent selectivity (CO Faradaic efficiency of 97%) and stability. DFT calculations reveals that the synthesized Fe-N_4-C can significantly reduce the energy barrier for intermediate COOH* formation and CO desorption. This work highlights the specific advantages of using electrospinning method to prepare the optimal SA catalysts.

Using renewable power to convert CO_2 into valuable products was an effective route to solve both environmental and energy shortage problems [1–3]. In the electrochemical reduction reaction of CO_2 (CO_2RR), realizing optimal activity, selectivity and stability were at the center of catalyst development. In recent years, heteroatom-doped carbon nanomaterials had become an effective catalyst for CO_2 conversion due to their low cost, excellent stability and large active area [4,5]. The interactions of heteroatoms in charge distribution, electronic properties, and defects could impact the chemical properties of the material thus providing more catalytic active centers [6,7]. The doping of heteroatoms (N, B, P *etc.*) and the introduction of metal atoms (Cu, Ni, Fe *etc.*) had realized the improvement of their electrocatalytic performance, especially the transition metal nitrogen unit (M-N_x) in carbon-based materials had advantages in electrocatalysis [8–10]. In addition, the metal centers binding to pyridinic-N and graphite-N in M-N-C were considered to be the reason for the formation of CO_2 to CO [11,12]. According to this theory, N-doped carbon nanotubes were prepared by vapor deposition method using acetonitrile and dicyandiamide as raw materials in Ar/H_2 atmosphere at 850 °C. The electrocatalytic selectivity reached 80% at 0.18 V. Compared with the precious metals Au and Ag, N-doped carbon nanotubes could efficiently convert CO_2 to CO at a lower potential. The experimental results showed that the initial potential and Faraday efficiency of CO formation varied with the content of pyridinic-N [13]. Aim to promote the CO_2RR performance, therefore, it was necessary to prepare M-N-C catalysts with more M-N_x, pyridinic N or graphite N active sites [14].

The use of carbon materials as carriers for M-N_x sites was one of the most important strategies due to their good electrical conductivity and stable electrochemical properties [15,16]. However, during the preparation of doped carbon-based electrocatalysts, high temperature pyrolysis of precursors tended to lead to the uncontrolled recombination in M-N_x, which led to the loss of M-N_x active center, the deterioration of mass transfer perfor-

* Corresponding authors.
E-mail addresses: hongliu@sdu.edu.cn (H. Liu), ifc_zhouwj@ujn.edu.cn (W. Zhou), chm_wangjg@ujn.edu.cn (J. Wang).
[1] These authors contributed equally to this work.

https://doi.org/10.1016/j.cclet.2024.110031
1001-8417/

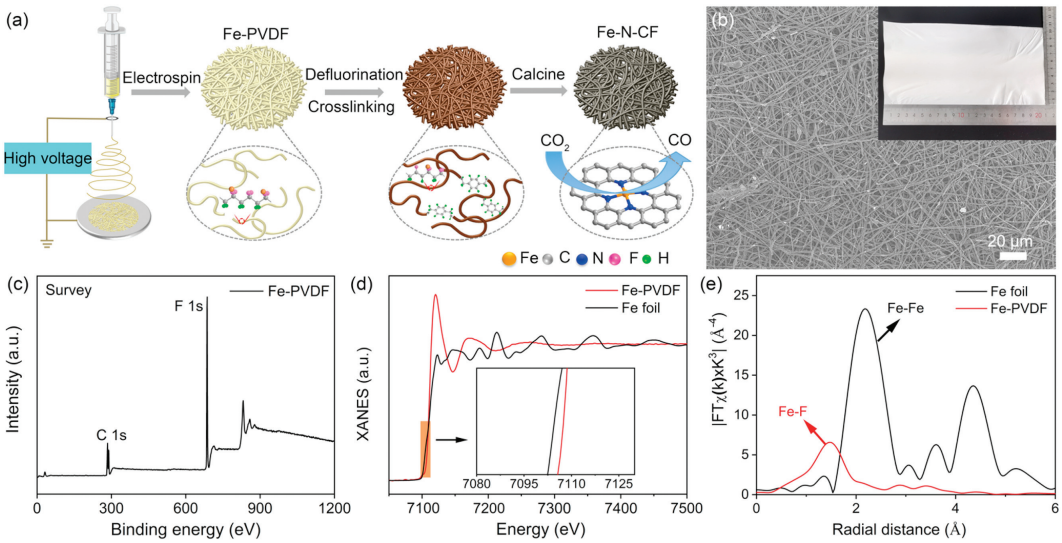

Fig. 1. (a) Schematic of the synthetic procedure of Fe-N-CF catalysts. (b) SEM image and digital image (inset) of the Fe-PVDF membrane. (c) XPS spectra of Fe-PVDF. (d) XANES spectra at the Fe K-edge and (e) the Fourier transform of EXAFS data for Fe-PVDF.

mance, and finally reduced the electrochemical properties [17,18]. Therefore, preventing metal atoms from recombination to obtain monatomic catalysts, increasing the density M-N_x active site and improving the mass transfer performance were effective routes to develop high performance CO_2RR electrocatalysts. In addition, the monolithic 3-dimensional (3D) porous carbon had unique advantages in CO_2RR due to their more catalytical sites, optimal electrical conductivity and high CO_2 mass transfer [19–21].

In this work, polyvinylidene fluoride (PVDF) fiber membranes mixed with Fe^{3+} were prepared by electrospinning. The stable scaffold structure was produced by defluorination and cross-linking of the nanofiber membranes, and then the 3D carbon nanofiber membranes with porous structure was obtained *via* pyrolysis in NH_3 atmosphere. The results showed that Fe existed as single atoms (SA) in the Fe-modified N-doped porous carbon fiber membrane catalyst (Fe-N-CF) and formed stable Fe-N_4-C structures with doped N. This self-supporting catalyst exhibited an excellent selectivity for the reduction of CO_2 to CO.

The Fe-N-CF catalyst was synthesized *via* a three-step process (Fig. 1a). Briefly, the Fe-PVDF precursor was prepared by electrospinning, followed by defluorination and cross-linking treatment, and finally Fe-N-CF catalyst was obtained by pyrolysis at 1000 °C in NH_3/Ar (1:2) atmosphere. Utilizing the electrospinning method enabled the preparation of large porous Fe-PVDF membrane, which was composed of nanofibers with diameters of 0.6-0.8 μm (Fig. 1b). XPS was performed on Fe-PVDF to investigate the surface properties, the results demonstrated the existence only of C and F (Fig. 1c). X-ray absorption fine structure (XAFS) measurement of Fe-PVDF was carried out to obtain the direct evidence for local chemical environment of Fe. The near-edge lines of Fe K-edge of Fe-PVDF was higher than that of standard Fe foil, indicating that the valence of Fe in Fe-PVDF was greater than 0. Besides, the Fourier-transformed k^3-weighted extended X-ray absorption fine structure (EXAFS) spectra of Fe-PVDF showed only one obvious peak at 1.47 Å, which was attributed to the coordination of Fe-F (Figs. 1d and e). F in PVDF could be regarded as hard base and could form stable coordination bond with hard acid (such as Fe^{3+}), which made Fe^{3+} monodisperse in PVDF. After defluorination process, C=C bonds were formed in the PVDF skeleton, and the network structures composed of C=C were formed by cross-linking reaction (Michael addition reaction) [22], which improved the thermal stability and mechanical strength of PVDF membrane. It was worth noting that there were still a large number of F elements in the defluorinated PVDF fiber (Fig. S1 in Supporting information), and these residual F are further removed in the form of –CF radicals in the subsequent pyrolysis process [22].

Fe-N-CF was obtained by calcination, which maintained the original 3D network structure, and the morphology of the fibers did not change significantly (Figs. 2a and b). The XRD pattern (Fig. 2c) indicated that only the diffraction peaks of C (PDF#26-1077). TEM image showed that a plenty of nanopores (bright parts) were on the surface and interior of nanofibers, which was due to the removal of –CF radicals during pyrolysis (Fig. 2d). The pore structure of Fe-N-CF was further investigated by N_2 adsorption-desorption experiments. The adsorption-desorption curves of Fe-N-CF showed an isotherm with type I and type IV properties, revealing the hierarchical porous structure of Fe-N-CF (Fig. S2 in Supporting information) [23]. The specific surface area of Fe-N-CF was 436 m^2/g. The pore size was mainly distributed less than 20 nm, which was consistent with the observed by TEM images. The HRTEM images showed the crystal structure of the carbon material, with clearly visible crystal plane spacing of 0.33 nm corresponding to the (005) plane of graphitic carbon (Fig. 2e) [24]. No crystal lattices of Fe were detected, which was consistent with the results of XRD. Furthermore, EDS elemental mapping (Fig. 2f) confirmed that C, O, N, and Fe elements were uniformly distributed along the carbon nanofibers, and no significant Fe enrichment was found. Compared with the defluorinated PVDF (Fig. S3 in Supporting information), the absence of F element indicated that the residual F atoms had been completely removed during pyrolysis. ICP-MS test (Table S1 in Supporting information) showed that the Fe amounts of Fe-N-CF was 0.14 wt%. Based on these results, the formation mechanism of Fe SA catalyst could be inferred. In the process of pyrolysis, with the overflow of -CF radicals, the vacancies were formed in the PVDF skeleton, as well as the N atoms occupied the vacancies and were embedded in the C skeleton. Simultaneously, Fe^{3+} were reduced by C during pyrolysis process, and the adjacent N atoms were combined with Fe by coordination bonds to form Fe-N-CF catalytic center.

To further analyze the Fe atoms on the catalysts, HAADF-STEM tests were performed. Due to the different Z contrasts of Fe, N, and C elements, it could directly distinguish Fe element from adjacent light elements [25]. Bright spots corresponding to heavy Fe atoms were observed, which was uniformly distributed in the carbon ma-

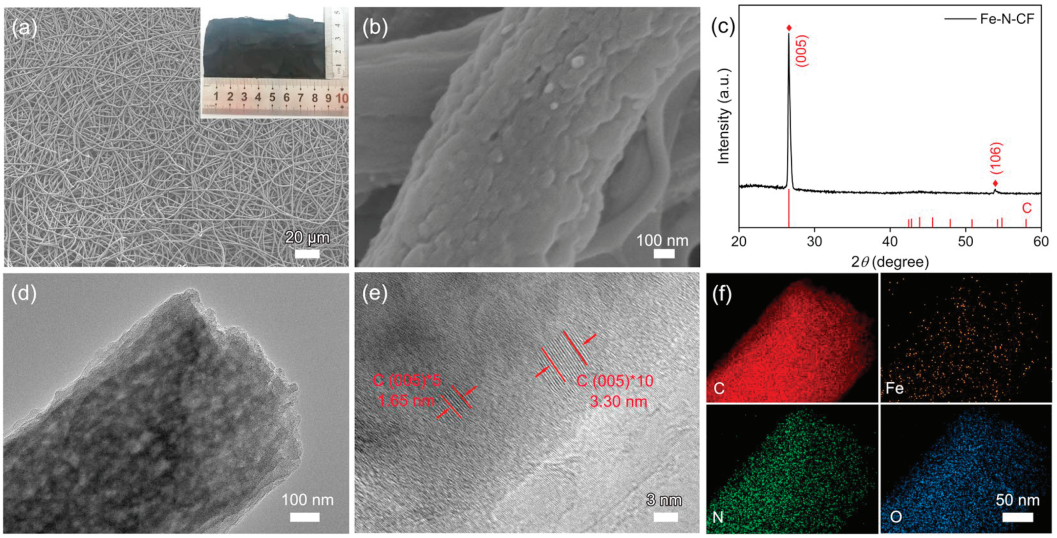

Fig. 2. (a, b) SEM images and digital image (inset), (c) XRD, (d) TEM, (e) HRTEM and (f) EDS elemental mapping of Fe-N-CF.

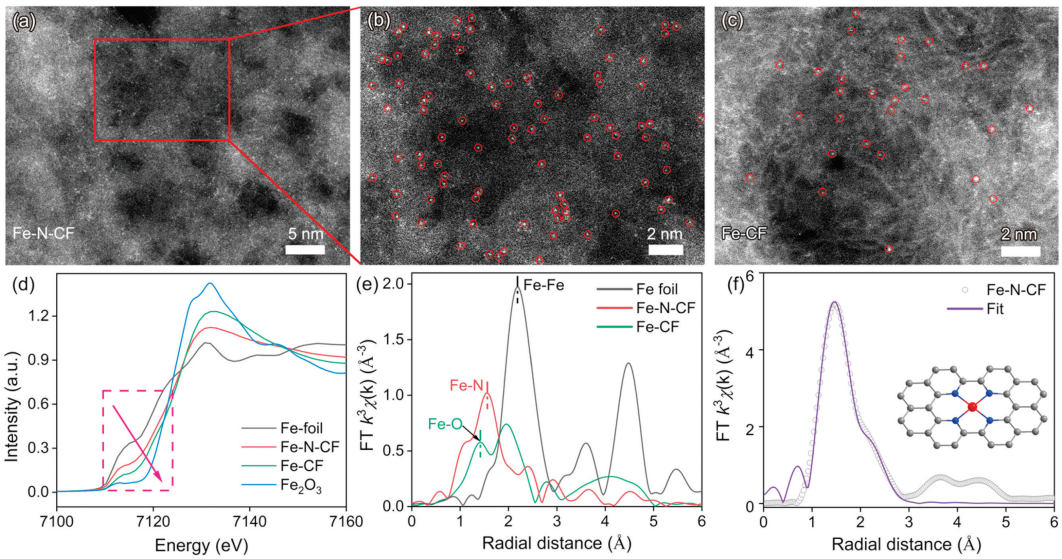

Fig. 3. (a, b) HAADF-STEM images of Fe-N-CF. (c) HAADF-STEM image of Fe-CF. (d) XANES spectra at the Fe K-edge and (e) the Fourier transform of EXAFS data for Fe foil, Fe-CF and Fe-N-CF. (f) Fitting for the EXAFS data of Fe-N-CF. Inset: the structure of Fe-N_4-C, Fe (red sphere), N (blue sphere), and C (gray sphere).

trix (Figs. 3a and b). A similar atomic-level distribution occurred on Fe-CF, only significantly less than for Fe-N-CF (Fig. 3c). The above results indicated that the special structure of PVDF-Fe could effectively avoid the aggregation of Fe atoms during pyrolysis, and the Fe SA were successfully prepared. Furthermore, Fig. 3d showed the X-ray absorption near-edge structure (XANES) spectrum in the Fe k-edge of Fe-N-CF and Fe-CF with Fe foil as reference materials. The near-edge spectrum of Fe-N-CF and Fe-CF located between Fe foil and Fe_2O_3, suggesting the average oxidation state of Fe was between Fe^0 and Fe^{3+} [26,27]. The fingerprint peak was around 7114 eV, indicating the existence of aquare-planar Fe-N_4-C species in the Fe-N-CF electrocatalyst [28,29]. Fig. 3e showed the Fourier-transform k^3-weighted $\chi(k)$ function of the EXAFS spectrum, it could be observed that there was only one peak in Fe-N-CF located at 1.56 Å corresponding to the Fe-N bond, which demonstrated that the isolated dispersion of Fe atoms on nitrogen-doped carbon supports. According to the fitting results, the local structure of Fe-N-CF involved to be Fe-N_4-C (Fig. 3f).

The elemental status of Fe-N-CF was discussed by various methods. First, the degree of defects of all catalysts was characterized by Raman spectroscopy (Fig. S4 in Supporting information). The Raman spectrum had two peaks at 1347 and 1578 cm^{-1}, which corresponded to disordered sp^3 carbon (D band) and graphite sp^2 carbon (G band), respectively [30]. The I_D/I_G intensity ratio of Fe-N-CF catalyst was significantly greater than that of Fe-CF, which indicated that Fe-N-CF had higher defect densities, thereby beneficial to the catalytic performance. XPS was then used to investigate the chemical state and surface composition of the as-prepared electrocatalysts. The typical XPS survey spectra showed that the Fe-N-CF electrocatalyst contained N, O, C, and Fe elements (Fig. S5 in Supporting information). The high-resolution N 1s spectrum of Fe-N-CF indicated the presence of pyridinic-N (398.3 eV), pyrrolic-N (399.69 eV), graphitic-N (400.99 eV), and oxidized-N (402.07 eV) species (Fig. S5b) [31,32]. The XPS results of the N-CF indicated that N in N-CF were mainly pyridine-N and graphite-N (Fig. S6 in Supporting information). Besides, the high-resolution O 1s spectrum of Fe-CF indicated the presence of Fe-O (Fig. S7 in Supporting information), which was consistent with the results of EXAFS.

The electrocatalytic activity of Fe-N-CF, Fe-CF and N-CF on CO_2RR were studied using a three-electrode H-cell. As shown by

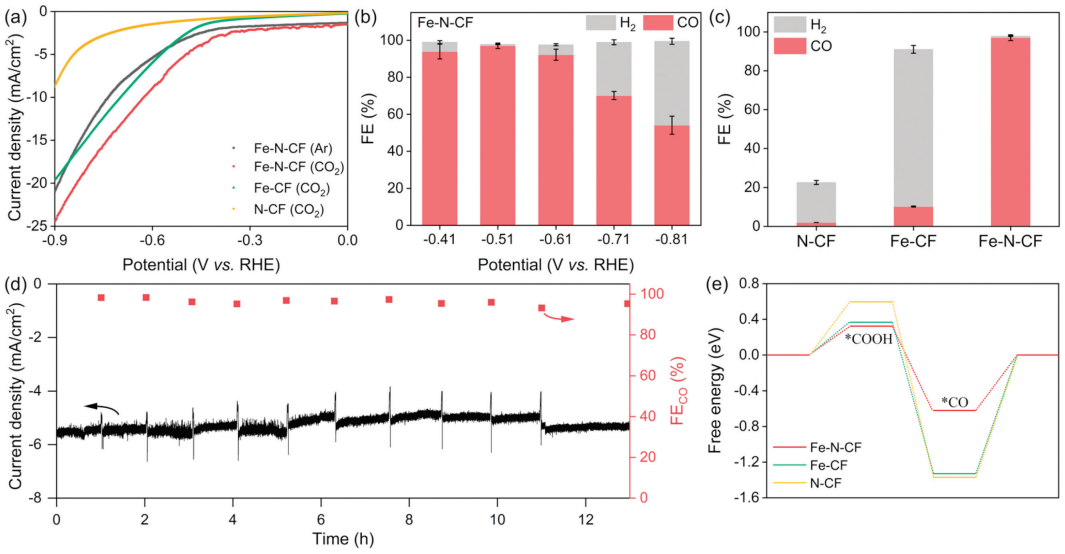

Fig. 4. (a) LSV curves of Fe-N-CF in Ar-saturated 0.5 mol/L $NaHCO_3$ solution and LSV curves in CO_2 saturated 0.5 mol/L $NaHCO_3$ solution of N-CF, Fe-CF and Fe-N-CF. (b) Faradaic efficiency of CO product in CO_2RR on Fe-N-CF at various cathode potentials. (c) Faradaic efficiency CO product in CO_2RR on N-CF, Fe-CF, and Fe-N-CF at −0.51 V_{RHE}. (d) Stability test of Fe-N-CF at −0.51 V_{RHE}. (e) Free energy for CO on Fe-N-CF, Fe-CF and N-CF, respectively.

LSV curves in Fig. 4a and Fig. S8 (Supporting information), for Fe-N-CF catalysts, a smaller current density and a higher onset potential were determined when tested in Ar-saturated $NaHCO_3$, which were caused by the reduction of protons to H_2. However, the larger current for CO_2RR was observed in the CO_2-saturated $NaHCO_3$ solution. The activity and selectivity were determined by constant potential electrolysis. Only CO and H_2 were detected over the whole investigated potential range. The faradaic efficiency of CO product (FE_{CO}) collected after one hour at different potentials were calculated (Fig. 4b). The as-prepared Fe-N-CF catalysts exhibited a high CO selectivity at low potentials ranging from −0.41 V_{RHE} to −0.61 V_{RHE}, with FE_{CO} of >90%, where Fe-N-CF could reach a maximum value of 97% at −0.51 V_{RHE}. By contrast, the FE_{CO} of Fe-CF and N-CF were extremely low (Fig. S9 in Supporting information), indicating the importance of the existence of Fe-N_4-C. At −0.51 V_{RHE}, the current density of Fe-N-CF was 5.42 mA/cm^2, which was significantly higher than that of N-CF and Fe-CF catalysts (Fig. S10 in Supporting information). The FEs of N-CF, Fe-CF, and Fe-N-CF at the optimal voltage of −0.51 V_{RHE} were shown in Fig. 4c, in which the selectivity of Fe-N-CF for reduction to CO was much higher than that of N-CF (FE_{CO} = 2%) and Fe-CF (FE_{CO} = 10.2%). The combination of results from XPS, XANFS and electroreduction data suggested that Fe-N was the main active site of Fe-N-CF. In addition, Fe-N-CF also exhibited excellent durability for CO_2RR, maintaining 95% of the initial FE for CO production (~5.3 mA/cm^2) during 13 h of continuous electrolysis at −0.51 V_{RHE} (Fig. 4d). There were no obvious changes occurred in the SEM image and XRD results after long-term test, which also illustrated the good stability of Fe-N-CF (Fig. S11 in Supporting information). Further, the Fe-N-CF appeared superior in the selectivity for CO product in CO_2RR as compared to other Fe-N_4 catalysts reported in recent years (Table S2 in Supporting information). These results suggested that the Fe-N_4-C species exhibited favorable activity and selectivity and was the decisive catalytic site on Fe-N-CF in CO_2RR, which was consistent with the reported results of M-N-C catalysts [33–35].

Density functional theory (DFT) calculations (section S1 in Supporting information) were performed to analyze the differences in the activities of the three prepared catalysts. In the reaction mechanism of CO_2RR to CO, COOH* and CO* were recognized adsorption intermediates [27], based on this, Fig. 4e depicted the free energy profiles (ΔG) of CO_2 electroreduction to CO. According to the simulation results, the first proton-coupled electron transfer of CO_2 to the adsorbed COOH* intermediate was the rate-determining step for all of these systems [36–38], where Fe-N-CF exhibited a more favorable ΔG (0.32 eV) than N-CF (0.60 eV) and Fe-CF (0.37 eV). Besides, compared with N-CF and Fe-CF, Fe-N-CF had a lower CO desorption free energy (0.62 eV). These results matched well with the experimental results that Fe-N_4-C structure presented improved activity and selectivity towards the conversion of CO product in CO_2RR.

In conclusion, we presented a rational design and facile synthesis to structure the atomically dispersed iron-anchored N-doped porous carbon nanofibrous membrane (Fe-N-CF) electrocatalysts. Due to the presence of F elements in the precursor and the subsequent nitriding treatment, the Fe-N-CF structure exhibited an excellent selectivity for CO product (Faradaic efficiency of 97%) and long-term stability at a small overpotential of −0.51 V_{RHE} in CO_2RR. DFT calculations revealed that Fe-N-CF significantly reduced the energy barrier for intermediate COOH* formation and CO desorption, which could rationalize the observed superior CO_2RR reactivity. This work provided a practical and efficient approach to develop 3D electrocatalysts at the atomic scale.

Declaration of competing interest

The authors declare that they had no known competing financial interests or personal relationships that could have appeared to influence the work reported in this paper.

CRediT authorship contribution statement

Xiujuan Wang: Writing – original draft, Methodology. **Yijie Wang:** Writing – review & editing, Data curation. **Luyun Cui:** Software. **Wenqiang Gao:** Writing – review & editing. **Xiao Li:** Methodology. **Hong Liu:** Supervision. **Weijia Zhou:** Supervision. **Jingang Wang:** Supervision, Methodology.

Acknowledgments

This work was financially supported by Construction Fund for the Collaborative Innovation Center of Biological Diagnosis and Treatment Technology and Equipment in Universities in Shandong

Province, City-School Integration Development Strategic Project of Jinan (No. JNSX2021015) and Shandong Province Key Research and Development Program (No. 2021ZDSYS18). The authors would like to thank Zhang Qian from Shiyanjia Lab (www.shiyanjia.com) for the HAADF-STEM analysis.

Supplementary materials

Supplementary material associated with this article can be found, in the online version, at doi:10.1016/j.cclet.2024.110031.

References

[1] R.C. Lu, X.Z. Zhang, H.X. Shi, et al., Appl. Catal. B: Environ. 341 (2024) 123293.
[2] H. Xue, H.L. Zhu, J.R. Huang, et al., Chin. Chem. Lett. 34 (2023) 107134.
[3] Y.L. Yang, Y.R. Wang, G.K. Gao, Chin. Chem. Lett. 33 (2022) 1439–1444.
[4] J. Han, X.M. Deng, K.Y. Chen, et al., Renew. Energy 177 (2021) 636–642.
[5] X.Y. Ma, J.J. Du, H. Sun, et al., Appl. Catal. B: Environ. 298 (2021) 120543.
[6] L.Y. Zhao, R. He, K.T. Rim, et al., Science 333 (2011) 999–1003.
[7] X.Y. Yi, H.J. Yang, X.X. Yang, et al., Adv. Func. Mater. 34 (2023) 2309728.
[8] F.F Chang, M.L Xiao, R.F. Miao, et al., Electrochem. Energy Rev. 5 (2022) 4.
[9] D. Ping, S.G. Huang, S.D. Wu, et al., Small 20 (2024) 2309014.
[10] D. Ping, Y.C. Feng, S.D. Wu, ACS Sustain. Chem. Eng. 12 (2024) 3034.
[11] M.H. Li, H.F. Wang, W. Luo, et al., Adv. Mater. 32 (2020) 2001848.
[12] D.F. Gao, T.F. Liu, G.X. Wang, X.H. Bao, ACS Energy Lett. 6 (2021) 713–727.
[13] P.P. Sharma, Electrochemical reduction of carbon dioxide on carbon nanostructures: Defect structures & electrocatalytic activity, Doctoral dissertation, University of South Carolina, 2016.
[14] T.T. Wang, J. Yang, J. Chen, Chin. Chem. Lett. 31 (2020) 1438–1442.
[15] J.J Wang, G.Q Cao, R.X. Duan, et al., Acta Phys. Chim. Sin. 39 (2023) 2212005.
[16] H. Sun, J.Y. Liu, Chin. Chem. Lett. 34 (2023) 108018.
[17] C.M. Zhao, X.Y. Dai, T. Yao, et al., J. Am. Chem. Soc. 139 (2017) 8078–8081.
[18] Y. Liu, Y.S. Fan, Z.M. Liu, Chem. Eng. J. 361 (2019) 416–427.
[19] B.X. Zhang, J.L. Zhang, F.Y. Zhang, et al., Adv. Funct. Mater. 30 (2020) 1906194.
[20] L. Ye, Y.R. Ying, D.R. Sun, et al., Angew. Chem. Int. Ed. 59 (2020) 3244–3251.
[21] Y. Zhang, H.L. Jiang, A. Kumar, et al., Carbon Energy 5 (2023) e341.
[22] D.Y. Koh, B.A. McCool, H.W. Deckman, R.P. Lively, Science 353 (2016) 804–807.
[23] S.D. Wu, J.M. Liu, B.B Cui, et al., Electrochim. Acta 299 (2019) 231–244.
[24] T.T. Wang, X.H. Sang, W.Z. Zheng, et al., Adv. Mater. 32 (2020) 2002430.
[25] Y. Zhu, X.Y. Li, X.P. Wang, et al., ChemistrySelect 5 (2020) 1282–1287.
[26] X.N. Li, X. Huang, S.B. Xi, et al., J. Am. Chem. Soc. 140 (2018) 12469–12475.
[27] K. Jiang, S. Siahrostami, T.T. Zheng, et al., Energ. Environ. Sci. 11 (2018) 893–903.
[28] Q.L. Zhu, W. Xia, L.R. Zheng, et al., ACS Energy Lett. 2 (2017) 504–511.
[29] N. Ramaswamy, U. Tylus, Q.Y. Jia, S. Mukerjee, J. Am. Chem. Soc. 135 (2013) 15443–15449.
[30] S.D. Wu, X.N. Lv, D. Ping, et al., Electrochim. Acta 340 (2020) 135930.
[31] H.J. Yang, X. Zhang, Y.H. Hong, et al., ChemSusChem 12 (2019) 3988–3995.
[32] L. Ye, Y.R. Ying, D.R. Sun, et al., Angew. Chem. Int. Ed. 59 (2019) 3244–3251.
[33] A.S. Varela, W. Ju, A. Bagger, et al., ACS Catal. 9 (2019) 7270–7284.
[34] L. Lin, H.B. Li, C.C. Yan, et al., Adv. Mater. 31 (2019) 1903470.
[35] N.M. Adli, W. Shan, S. Hwang, et al., Angew. Chem. 133 (2021) 1035–1045.
[36] Q. Zeng, S.N. Tian, H. Liu, et al., Adv. Funct. Mater. 33 (2023) 2307444.
[37] J.Y. Chen, Z.J. Li, X.Y. Wang, et al., Angew. Chem. Int. Ed. 61 (2022) e202111683.
[38] X.Z. Fu, P.P. Zhang, T.T. Sun, et al., Small 18 (2022) 2107997.